*metals*

MDPI

*Article*

# Analysis of Fatigue Strength of L-PBF AlSi10Mg with Different Surface Post-Processes: Effect of Residual Stresses

**Francesco Sausto, Christian Tezzele and Stefano Beretta ***

Department of Mechanical Engineering, Politecnico di Milano, Via La Masa 1, 20156 Milan, Italy; francesco.sausto@polimi.it (F.S.); christian.tezzele@mail.polimi.it (C.T.)

* Correspondence: stefano.beretta@polimi.it

**Abstract:** Space and aerospace industries has been starting in the recent years the replacement process of parts and components obtained by traditional manufacturing processes with those produced by Additive Manufacturing (AM). The complexity of the obtainable parts makes, in general, challenging the superficial post processing of some zones, making a stringent requirement the investigation of the fatigue performances of components with rough superficial state or machined. The aim of this work is then to analyse and compare the fatigue performances of an additively manufactured (AMed) AlSi10Mg material considering both the effects of the manufacturing defects and residual stresses related to three different superficial states, namely machined, net-shape and sandblasted. The residual stress profiles of the three superficial states were found to play a key role in determining the fatigue properties of the analysed material, while the manufacturing defects at the failure origin were found to be comparable among the three series. To take into account the combined effect of residual stresses and manufacturing defects a fracture mechanics approach was considered for the estimation of the fatigue performances in both infinite and finite life regimes. It was found that by considering the nominal measured residual stress profiles in the fracture mechanics model the estimations were satisfactory compared to the experimental data-point. To increase the accuracy of the fatigue life estimations a series of numerical analyses were performed aimed to investigate the residual stresses relaxation during the cyclic loading. The adoption of the relaxed residual stress profiles in the fracture mechanics model resulted in good estimations respect to the experimental data-points, highlighting the necessity in adopting such developed approaches during the design phase of AM parts and components.

**Keywords:** additive manufacturing; laser powder bed fusion; fatigue strength; residual stresses; fracture mechanics approaches



**Citation:** Sausto, F.; Tezzele, C.; Beretta, S Analysis of Fatigue Strength of L-PBF AlSi10Mg with Different Surface Post-Processes: Effect of Residual Stresses. *Metals* **2022**, *12*, 898. https://doi.org/10.3390/met12060898

Academic Editors: Yves Nadot, Jean-Yves Buffière and Franck Morel

Received: 19 April 2022
Accepted: 20 May 2022
Published: 25 May 2022



## 1. Introduction

In a market pushed by a constantly growing demand of highly customizable and complex-shaped components, Additive Manufacturing (AM) is playing an increasingly relevant role due to its greater flexibility with respect to the traditional subtractive processes. The layer-wise part's creation allows achieving strength-optimised structures in a relatively short time, guaranteeing high structural performances, low mass and material saving [1–3]. Despite the offered advantages, metal AMed components feature high surface roughness, internal and superficial defects, anisotropy and residual stresses which cause deleterious effects on the fatigue performances [4–6].

Fracture mechanics approaches revealed to be prospectively accurate tools able to account for the synergetic effect of those process-induced criticalities, using a damage tolerant approach to model the fatigue strength [7–15]. Independently from their morphology, defects can be treated as cracks according to the Murakami's $\sqrt{area}$ parameter, and the location's influence is introduced by means of a geometry factor [16]. The fatigue strength in function of the defect size is then described implementing the Kitagawa-Takahashi diagram

and introducing the El-Haddad's formulation [17] to provide a smooth transition between long and short cracks' behaviour. The tool has also proved to be effective in accounting for the superimposed residual stress component, as long as the measurements provided are accurate and characterised by low scatter [18,19].

In these terms, several studies have shown the key role played by the residual stresses in affecting the fatigue performances, especially in the High Cycle Fatigue (HCF) range [9,20]. The residual stress component superimposes to the cyclically applied ones, thus modifying the stress ratio experienced by the material. The former directly acts on the crack growth behaviour, determining an either beneficial or detrimental effect if the superimposed stresses tend to close or open the crack's faces [21,22] respectively. At the actual state of the art, the requirement of obtaining accurate and precise measurements is everything but easy to achieve, nominating residual stresses as the weakest link in the assessment of AMed components.

Concerning metal AM processes, the usage of a high energy density heat source subjects the component's regions to thermal misfits [23]. During the production phase, in Laser Powder Bed Fusion (L-PBF) the large thermal gradients, high temperatures and material phase transition generally induce local plasticisation and shrinkage, which are responsible for the introduction of residual stresses [24]. Those stress components are in place even if the part is in stationary conditions and in equilibrium with the external environment [25]. Their magnitude and spatial distribution are strictly dependent on the thermal history experienced by the material, affected in turn by process parameters and part's geometry [26]. Techniques used for the investigation generally require an important amount of time and involve a significant economic burdens, associated with a locally-limited analysis which prevents obtaining a complete framework in terms of stress' spatial distribution and magnitude [27]. Additional factors to be considered are the geometry-limited accessibility and the destructive nature of some methods.

The tensile residual stresses generally present in the superficial material layers of L-PBFed components increase the vulnerability of such locations, already critically affected by the surface features typically found in the as-built state [28]. Efforts have been made in order to try mapping the residual stresses by implementing Finite Element (FE) thermo-mechanical models which are able to reproduce the thermal history experienced by the material during the process [29]. Nonetheless, the approach is generally limited by large computational burdens, and the unavoidable introduced simplifications lead to inaccuracies in the temperature field computation [30,31].

Numerous studies have attempted to tackle the problem by properly adjusting the process parameters, aiming at minimizing the tensile residual stress component. In these terms, variables comprising the beam's power, scanning speed and strategy, layer thickness, base plate temperature, interlayer dwell time, building direction, presence of supports and many others are all able to play a key role [28,32–34]. Although relevant improvements have been achieved, post-processes both of thermal and mechanical nature are still needed in order to modify the residual state of stress, with the aim of improving the fatigue performances [35,36]. In the case of additively manufactured (AMed) AlSi10Mg, it was shown that the T6 heat treatment process was able to increase the fatigue strength of both machined [37] and net-shape specimens [38]. Particularly for the net-shape specimens investigated by Domfang et al. [38], the size of the found defects was comparable to that of machined specimens, and therefore, the fatigue strength of the two T6-treated specimens' series was similar. Even if the residual stresses of treated and non-treated specimens were not measured, the authors pointed out that they can play an important role in explaining the obtained experimental results.

The potential relaxation of residual stresses under cyclic loading consists of a further factor of complexity to account for in a fatigue strength model. This phenomenon has not been thoroughly investigated for L-PBFed parts, while it has been well-studied in welds [39,40], which share some analogies with AM processes. The relaxation is the result of a local plasticisation, therefore information about the in-depth residual stress profile,

cyclic stress and material's plastic behaviour are needed in order to to properly model the phenomenon [41]. Additionally, it should be noted that a local relaxation of residual stresses is associated with a redistribution of the entire residual stress profile in order to ensure equilibrium. It appears therefore worthwhile to broaden the understanding related to the effect of post-processes on the residual state of stress and the consequent influence on the fatigue performances.

*Scope of the Work and Paper Structure*

The main aim of the present work consists of studying the fatigue strength of specimens in AlSi10Mg manufactured by L-PBF, considering net-shape, machined and sandblasted surface conditions in light of the superimposed residual stress component. For this purpose, fracture mechanics-based approaches have been implemented allowing to account for the synergetic effect of process-induced criticalities comprising both residual stresses and manufacturing defects. The relaxation of residual stresses under cyclic loading has been modelled through FE analyses starting from the experimental measurements, and adopting a proper cyclic plasticity model. The agreement among the obtained results and experimental evidence confirmed that fracture mechanics consists of a prospective tool able to model the fatigue strength of components subjected to different post-processes, provided that the residual stress' redistribution under cyclic loading is considered.

The paper is organised as follows: in Section 2 the adopted technological process for the fabrication of the specimens as well as the experimental methodologies are described; Section 3 presents the main results coming from the experimental tests of the fatigue specimens; the numerical analysis of the residual stress profiles, experimentally measured, aimed to investigate their prospectively relaxation is presented and discussed in Section 3; in Section 5 the fatigue model based on the fracture mechanics approach are described and adopted for the estimation of the fatigue tests results; Section 6 deals with the main conclusions and further developments.

## 2. Materials and Methods

The experimental campaign involved specimens to be tested in both force and strain control logic; specimens were AMed in AlSi10Mg by laser powder bed fusion (L-PBF). Samples were produced using an selective laser melting (SLM) 280HL v1.0 machine (SLM Solutions Group AG, Lübeck, Germany) having a $280 \times 280 \times 350$ mm$^3$ volume building chamber equipped with $2 \times 400$ W Yttrium fibre lasers. The process was carried out in controlled atmosphere using argon to reduce the oxygen content down to 0.2%. Set parameters comprised a beam power of 350 W, a hatch distance of 0.13 mm, a scanning speed equal to 1650 mm s$^{-1}$ and a layer thickness of 50 µm resulting in an energy density of 32.63 J mm$^3$. Stripes scanning mode characterised by 67° layer rotation was used with a scanning order consisting in two contours followed by the hatch scanning. During the entire manufacturing process, the building platform's temperature was kept at 150 °C. These process parameters are the standard ones adopted by the company that provided the specimens adopted in this study, BeamIT S.p.A. (Fornovo di Taro (PR), Italy). The AlSi10Mg powder produced by ECKA (ECKA Granules GmbH, Velden, Germany) was characterised by granules having a mean size of 37 µm, a $D_{10}$ and $D_{90}$ respectively equal to 21 µm and 65 µm, with a flowability of 80 s/50 g. Prior to removing the specimens from the platform by means of an electric discharge machining, all samples were subjected to a T5-heat treatment involving a temperature of 200 °C and a soaking time of 240 min.

Net-shape and sandblasted specimens were produced without any material overstock in the gauge section, providing it exclusively in correspondence of the gripping zones, a 0.2 mm of extra material, which was mechanically removed by means of a lathe to ensure specific geometric and dimensional tolerances. For machined parts, the same material overstock and subsequent machining was prescribed for the entire sample's length, thus comprising the gauge section which was additionally polished using emery paper with a mesh ranging from 250 to 2500 for obtaining a smooth surface roughness.

Specimens were vertically printed as schematically shown in Figure 1, where the lower gripping section was 30 mm longer than the upper one, thus allowing further machining in order to achieve the final length as displayed in Figure 1b,c, for the strain and force control test's specimens respectively. Prior to testing, sandblasted parts were subjected to an additional sandblasting process.

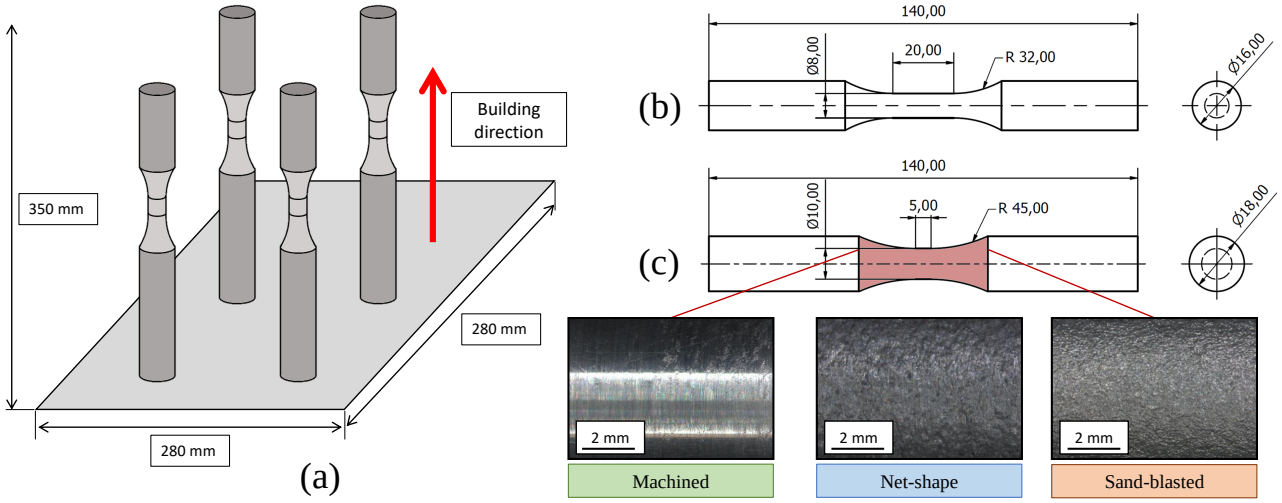


**Figure 1.** Printed specimens for the experimental campaign: (**a**) printing direction; (**b**) strain controlled fatigue tests' specimen geometry according to the American Society for Testing Materials (ASTM) standard E606 [42] and (**c**) force control fatigue tests' specimen geometry with a detail of the three different superficial conditions. All the dimensions are in mm.

### *2.1. Fatigue Tests*

Samples were subjected to uniaxial force-controlled fatigue tests at room temperature using a servo-hydraulic MTS-810 (MTS System Corporation, Eden Prairie, MN, USA) machine with a maximum capacity of 100 kN, imposing a global load ratio $R_L = -1.0$ being the basic requirements of ECSS-Q-ST-70- 80C standard [43]. Each test terminated with the final rupture of the specimen, with a final crack length of 4.5 mm, on average. Specimens that survived beyond $5 \times 10^6$ cycles were considered as *Run-Outs* and, in absence of any visible damage, they were subsequently retested at higher stress ranges in order to reach the final rupture and analyse the defect at the fracture origin. The exact failure location identified with respect to the sample's geometry was used in a finite element elastic analysis, allowing to obtain the actual stress range responsible for the fatigue crack propagation. Table 1 summarizes the performed tests with the related series' code that will be used throughout this paper.

**Table 1.** Overview of fatigue tests performed on machined, net-shape and sandblasted samples.

| Series' Code | Surface State | Global Load Ratio | Number of Tests |
|---|---|---|---|
| M | Machined | −1.0 | 12 |
| NS | Net-shape | −1.0 | 29 |
| SAB | Sandblasted | −1.0 | 19 |

### *2.2. Strain Control Fatigue Cyclic Tests*

Three of the printed specimens were machined in order to obtain the geometry shown in Figure 1b. This is compliant with the specifics for strain controlled tests as reported in standard ASTM E606 [42]. The specimens were tested at ambient temperature in order to obtain the cyclic parameters of the considered AlSi10Mg material. The same hydraulic testing machine adopted for the force control tests was adopted for the strain controlled tests. Five strain amplitudes were applied in blocks considering a strain ratio of $R_\varepsilon = -1.0$,

namely 0.2%, 0.4%, 0.5%, 0.6% and 0.7%. Each test started with the lower strain amplitude which was then increased after the stabilization of the cyclic curve.

### *2.3. Residual Stress Measurements*

Machined, net-shape and sandblasted specimens were subjected to residual stress investigations using a X-Stress 3000 American Stress Technology (AST, Pittsburg, PA, USA) portable X-ray diffractometer equipped with a 2 mm diameter collimator, with a CrK$\alpha_1$ radiation characterised by a wavelength of 2.2898 Å. A $\sin^2 \psi$ method was adopted and a diffraction angle $2\theta = 139.3°$ was fixed after the calibration procedure with a stress-free aluminium powder. The angular scanning aperture was set ranging in $\pm 45°$, with a total number of 16 tilts. Electrolytic polishing was performed by means of a Struers LectroPol-5 (Struers LLC, Detroit Rd. Westlake Cleveland, OH, USA), with a voltage of 45 V and using a fluid-directing mask characterised by a 0.5 $cm^2$ circular area. The electrolytic solution adopted consisted in 94% of acetic acid ($CH_3COOH$) and 6% of perchloric acid ($HClO_4$). The erosion time was adjusted for each individual specimen for guaranteeing the target step depth, which was measured by means of a Mitutoyo (Mitutoyo Corporation, Takatsu Ward, Kawasaki, Japan) Litematic VL-50A micrometer.

Residual stresses were investigated along the building direction in the longitudinal ($\Theta = 0°$) and transversal ($\Theta = 90°$) orientations, in correspondence of the gauge section's central part. Machined and net-shape samples were measured along three generatrices equally spaced at an angle equal to 120°, while in the case of sandblasted specimens only two generatrices were considered, each spaced at 180°.

Machined specimens were inspected superficially (0 µm depth), followed by in depth measurements at 50 µm and 100 µm. Net-shape specimens were inspected considering the same depths of machined ones, with two deeper analyses at 300 µm and 500 µm. In sandblasted specimens the maximum achieved nominal depth was about 400 µm, reached performing a first superficial measurement (0 µm), one at 50 µm followed by 100 µm erosion steps.

### *2.4. Fracture Analysis*

Failed specimens' fracture surfaces were sonicated in ethanol prior to carrying out an accurate analysis by means of a Zeiss EVO50 (Carl Zeiss AG, Oberkochen, Germany) scanning electron microscope (SEM). The investigation allowed to identify the defects at fracture origin and define the related position, shape and characteristic dimensions.

## 3. Results

### *3.1. S-N Curves*

Figure 2 shows the comparison of the HCF tests' results among machined, net-shape and sandblasted specimens; the whole experimental results set of net-shape and machined specimens can be found in [18]. Some additional tests on net-shape specimens, especially at higher stress ranges, were also performed to increase the experimental data-base reported in [18]. A three-parameters Gaussian distribution was used for the data fitting in the finite life region, imposing a constant standard deviation $\sigma_{\log N}$. Equation (1) reports the expression of the distribution's mean value, as prescribed by ASTM E739 [44].

$$N_f = A \cdot \Delta\sigma^B \tag{1}$$

where $N_f$ is the number of cycles to failure, $\Delta\sigma$ coincides with the applied stress range, while $A$ and $B$ correspond to the distribution's parameters identifying respectively the vertical axis' intercept and the regression line's slope in a double logarithmic plot. Hodge-Rosenblatt [45] method was used to compute the fatigue limit range's mean value $\Delta S_{lim}$, and the related standard deviation was calculated relying on Equation (2).

$$\sigma_{\log S} = \frac{\sigma_{\log N}}{|B|} \tag{2}$$

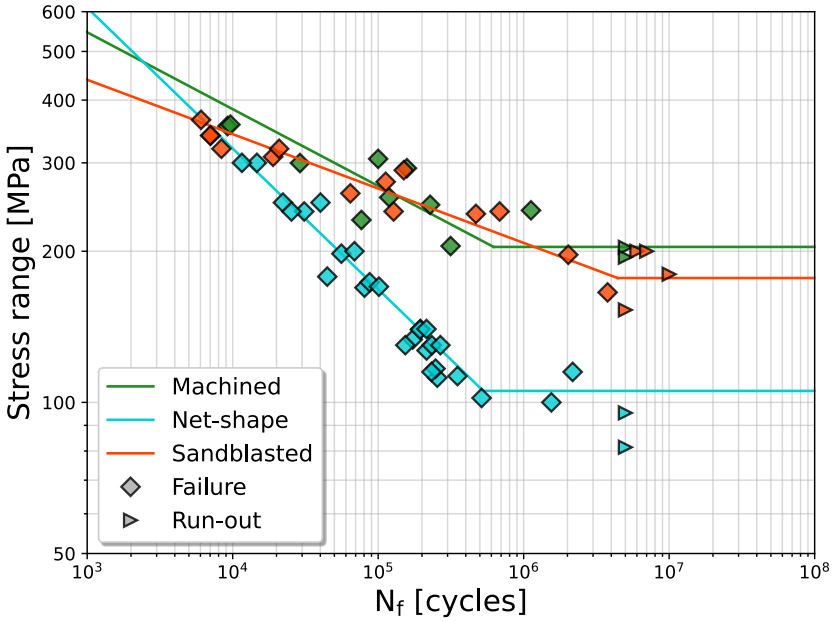


**Figure 2.** Comparison of the results of the fatigue tests of machined, sandblasted and net-shape axial specimens. Stress range has to be intended as maximum stress minus the minimum one during the fatigue cycle.

Table 2 collects the distributions' parameters of the three tested series, where $N_k$ refers to the S-N curves' knee point.

**Table 2.** Fatigue limit range and S-N curves' parameters related to machined, net-shape and sandblasted samples.

| Series' Code | $\Delta S_{lim}$ [MPa] | $A$ | $B$ | $\sigma_{\log N}$ | $\sigma_{\log S}$ | $N_k$ [Cycles] |
|---|---|---|---|---|---|---|
| M | 204.0 | 26.1473 | −8.6478 | 0.2632 | 0.0304 | 1,490,399 |
| NS | 105.4 | 12.1314 | −3.2196 | 0.0955 | 0.0297 | 415,666 |
| SAB | 176.9 | 30.4444 | −10.4728 | 0.2544 | 0.0243 | 8,043,806 |

From the fatigue limit point of view, machined specimens are characterised by the highest value which is about 94% larger than the one of net-shape parts featuring the lowest performances. The sandblasting post-process was able to enhance the fatigue properties of about 68% with respect to the net-shape specimens, making their fatigue performances close to the ones of machined samples. In these terms, in the finite life region machined and sandblasted specimens show a certain similarity of the regression line's slope, while the trend related to net-shape parts presents relevant differences with respect to the other two series. These discrepancies are visible especially for relatively low applied stress ranges, highlighting the beneficial effects provided by the two mechanical processes. On the contrary, at large values of stress the data-points of the three batches are superimposed. Since the three specimens series were obtained with the same process, and therefore the size of internal defects due to L-PBF process is expected to be the same, it is clear that the significant increase of fatigue properties for sanblasted specimens can be due the induced residual stresses. The aim of the research was to investigate this effect and to verify if the increase of properties could be adequately modelled with a fracture-based approach [13].

### *3.2. Analysis of Fracture Surfaces*

Figure 3 shows some of the fracture surfaces observed in tested samples, where the yellow path highlights the killer defect. In machined specimens, defects found at fracture origin were all located near the external surface. They consisted in lack of fusions (LoFs)

characterised by irregular shapes and gas pores defined by a spherical shape, as reported in Figure 3A and Figure 3B respectively.

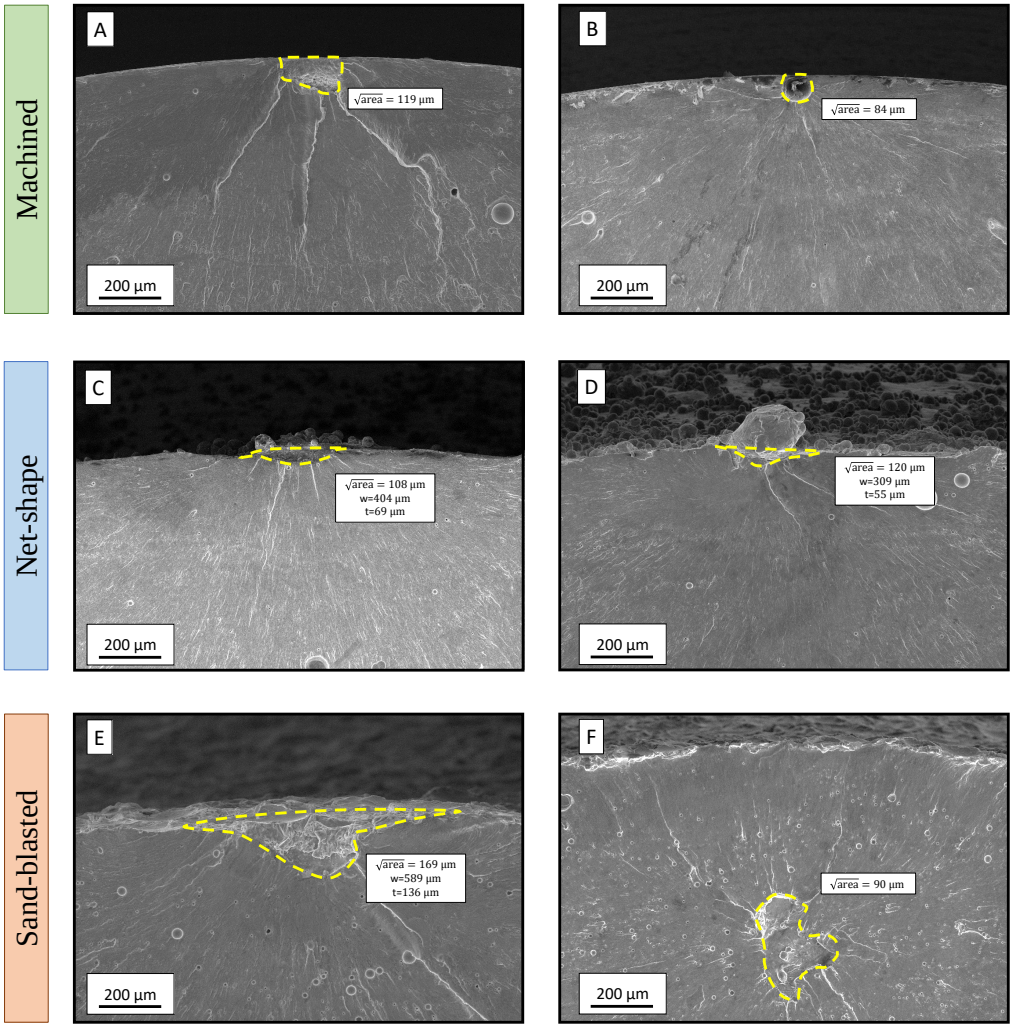


**Figure 3.** Defects found at fracture origin in machined, net-shape and sandblasted specimens: (**A**) LoF and (**B**) gas pore; (**C**) surface irregularity and (**D**) SPP; (**E**) superficial feature and (**F**) internal LoF.

Net-shape specimens failed mainly due to surface features, which are typical of the rough external surface as shown in Figure 3C and spherical powder particles (SPP) as displayed in Figure 3D. In only one specimen of this series an internal gas pore was responsible for the final rupture.

Killer defects detected in sandblasted specimens included surface features (Figure 3E), and LoFs (Figure 3F). The fact that approximately one third of the flaws were positioned in the internal material layers, reveals how the induced residual stresses compete in defining the fatigue crack initiation site.

### *3.3. Residual Stresses Measurements*

Figure 4a,b display the comparison of residual stresses measured in machined, net-shape and sandblasted specimens, respectively along the longitudinal ($\Theta = 0°$) and transversal ($\Theta = 90°$) directions, referred as $Z$ and $X$ axes according to the reference system shown in Figure 4c. The solid lines are obtained by means of a polynomial fitting of the experimental data related to each series.

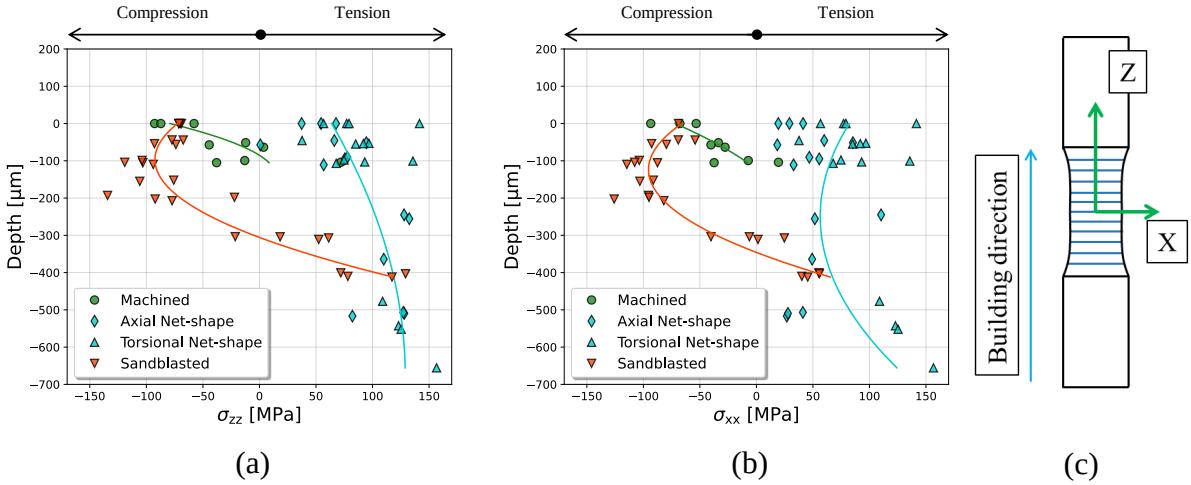


**Figure 4.** Comparison of measured residual stresses of machined, net-shape and sandblasted components: (**a**) $\sigma_{zz}$; (**b**) $\sigma_{xx}$; (**c**) schematic of the measuring directions.

Along both the inspected orientations, machined samples are characterised by a compressive residual state of stress in the first material layers, down to a depth of about 100 µm. In correspondence of the external surface, an average stress of approximately −79 MPa and −72 MPa was detected respectively along *Z-axis* and *X-axis*, noticing a monotonic increase towards tensile values for both of the directions. The resulting trend is typical of components subjected to chip removal processes [46].

Conversely to the machined parts, net-shape specimens are characterised by the presence of tensile residual stresses for the whole inspected depth along the two analysed orientations. As extensively reported in literature, the large thermal gradient the material experiences during the layer-by-layer manufacturing process induces tensile residual stresses in the outer layers [9,13,18]. In these terms, the platform pre-heating and the T5-heat treatment were not able to effectively relieve the process-induced stresses. On the external surface, average stresses of about $\sigma_{zz} = 73$ MPa and $\sigma_{xx} = 64$ MPa are present, and it can be noticed how the data dispersion is relevant for certain depth increments.

Sandblasted specimens featured a quite similar trend along the two inspected axes, where the residual stresses are compressive in correspondence of the external surface reaching a minimum at about 200 µm, moving then to the tensile part after approximately 300 µm. The shape of the stress profile coincides with the characteristic one induced by kinetic surface treatments [35]. In correspondence of the surface, the mean values are about $\sigma_{zz} = -70$ MPa and $\sigma_{xx} = -69$ MPa, which are comparable with the machined samples' ones.

For relatively large depths, the tensile residual stresses measured in net-shape and sandblasted specimens reach relevant magnitudes which are comparable to the yield strength of the material $R_{p,0.2\%} = 212$ MPa [18]. Considering that all the defects found at fracture origin were located either in correspondence of the surface or in the substrate, it is evident how the superimposed residual stress component was able to affect the effective stress ratio, thus influencing the fatigue performances.

The whole experimental database of the residual stresses measurements for machined and net-shape specimens is reported elsewhere [18], while the results obtained for sandblasted specimens are reported in the Appendix A.

### *3.4. Defect Distributions and Statistics of Extremes*

In AMed components, the key role played by manufacturing-induced defects in affecting the fatigue performances, leads to the adoption of fracture-mechanics based methods [7,8]. Accordingly, the approach proposed by Murakami [16] was used to define the killer defect's size in terms of $\sqrt{\text{area}}$ independently from its shape, where area refers to

the projected surface of the flaw which has been measured through an image processing software [47]. Flaw's location was defined applying Equation (3), which sets the condition for having a superficial defect. The quantity $h$ identifies the distance between the defect's centroid and the sample's surface [16]. The term $a$ is computed through Equation (4), corresponding to the length of the axis pointing inside the material depth of an equivalent ellipse which has the same defect's area and an aspect ratio $AR = a/c$.

$$\frac{a}{h} > 0.8 \tag{3}$$

$$a = \sqrt{\frac{2 \cdot AR}{\pi}} \cdot \sqrt{\text{area}} \tag{4}$$

Equation (5) describes those superficial elongated and shallow defects which tend to behave like 2D edge cracks, having identified with $w$ and $t$ the flaw's width and depth, respectively. In these terms, the related effective area was calculated by means of Equation (6), where $t_{\max}$ is the maximum depth of the defect.

$$\frac{w}{t} \geq 10 \tag{5}$$

$$\sqrt{\text{area}} = t_{\max} \cdot \sqrt{10} \tag{6}$$

A schematic of the main parameters that identify the superficial and internal defects is reported in Figure 5a. The main part of the defects found were located near the external specimen's surface, while few of them were internal, comprising both LoFs and pores as shown in Figure 5b. In Figure 5c the square root area $\sqrt{\text{area}}$ parameter of the found defects at the fracture origin of the tested specimens, is plotted against their aspect ratio $a/c$. Defects found inside the machined specimens showed an aspect ratio above or equal to $a/c = 1.0$. Net-shape and sandblasted specimens were found to fail mainly due to superficial elongated defects, with a mean aspect ratio $a/c = 0.25$. This is in line with a typical aspect ratio of defects at the fracture origin of other AMed materials featured with a rough superficial state [11,12].

The complexity of phenomena involved in the production of AMed components and parts introduces sources of uncertainty, requiring the adoption of statistical models [7]. The inspected defects were responsible of the final failure of the specimens, therefore it is possible to study the flaw size distribution applying the statistics of extreme [48,49]. Data were hence fitted with a largest extreme value distribution (LEVD) [50], characterised by a cumulative distribution function reported in Equation (7):

$$F_{\max}(x) = \exp\left[-\exp\left(-\frac{x-\lambda}{\delta}\right)\right] \tag{7}$$

where $x$ is the defect's size in terms of $\sqrt{\text{area}}$, while $\lambda$ and $\delta$ are, respectively, the estimated location and scale parameters. Table 3 collects the distribution's parameters computed using the momentum equations [50], together with the defect size having a 50% probability of occurrence ($\sqrt{\text{area}}_{50\%}$).

**Table 3.** LEVD distribution parameters for machined, net-shape and sandblasted specimens.

| Series' Code | $\lambda$ [µm] | $\delta$ [µm] | $\sqrt{\text{area}}_{50\%}$ [µm] |
|---|---|---|---|
| M | 96.1 | 49.3 | 114.2 |
| NS | 99.6 | 30.5 | 110.8 |
| SAB | 116.7 | 33.2 | 128.8 |

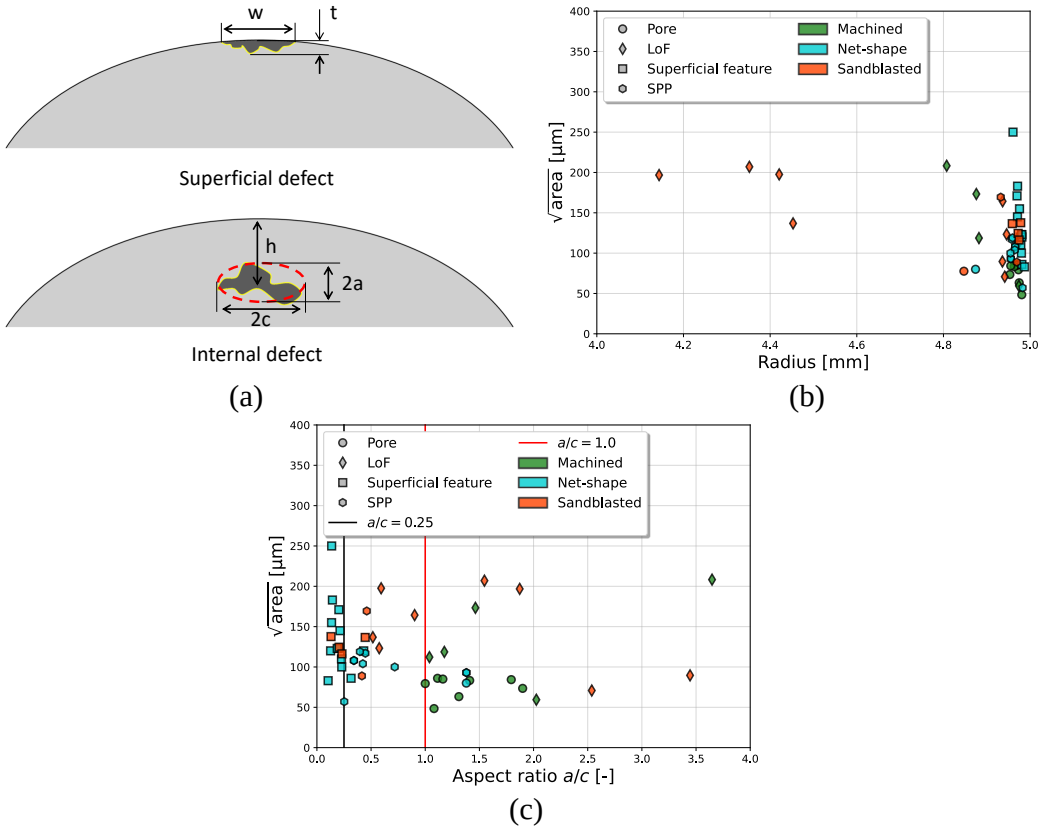


**Figure 5.** Analysis of the size and geometry of the found defects: (**a**) scheme of the main parameters that define superficial and internal defects; (**b**) dimension of the defects against its radial position and (**c**) dimension of the defects against its aspect ratio.

A slight difference among the slope of the regression lines related to net-shape and sandblasted specimens can be detected from the different $\delta$ parameters, which rule the line's inclination in the probability plot. Conversely, for machined specimens the trend is less steep while all the three series share a similar value of the position parameter $\lambda$. A further analogy can be found in the $\sqrt{\text{area}}_{50\%}$ factor, highlighting how the three distributions are comparable from a statistical point of view.

### *3.5. Cyclic Plasticity Material Model*

To investigate the evolution of residual stresses during a typical fatigue loading, the plastic behaviour of the considered AlSi10Mg alloy has to be determined. To this aim three strain controlled tests were performed, by imposing consecutive strain amplitude blocks.

From the hysteresis cycles, the stabilized stress and strain amplitudes can be computed. These were then fitted with the Ramberg–Osgood cyclic curve [51], whose expression is reported in Equation (8):

$$\varepsilon_a = \varepsilon_{a,el} + \varepsilon_{a,pl} = \frac{\sigma_a}{E_{stab}} + \left(\frac{\sigma_a}{K'}\right)^{(1/n')} \tag{8}$$

where $\varepsilon_{a,el}$ is the elastic strain amplitude, $\varepsilon_{a,pl}$ is the plastic strain amplitude, $\sigma_a$ is the stress amplitude and $E_{stab}$ is the stabilized Young's modulus; $K'$ and $n'$ are the hardening coefficient and exponent of the plastic part of the stabilized cyclic curve, respectively. The results of the fitting are reported in Table 4.

**Table 4.** Parameters of the cyclic curve of AlSi10Mg alloy.

| $E_{stab}$ [GPa] | $K'$ [MPa] | $n'$ [-] |
|---|---|---|
| 73.7 | 852.5 | 0.2218 |

In order to numerically simulate the elasto-plastic behaviour of the material considered, a suitable cyclic plasticity model has to be fitted with the experimental results; to this aim the Chaboche cyclic plasticity model [52] was adopted. The material does not manifest any marked cyclic hardening or softening, resulting in a mainly stable cyclic behaviour. Due to this observation, only the kinematic hardening model was considered. The adopted kinematic rule is reported in Equations (9) and (10), more details about the theory of the Chaboche model can be found in [52].

$$d\underline{\alpha}^k = \frac{2}{3} \cdot C_k \cdot d\underline{\varepsilon}^p - \gamma_k \cdot \underline{\alpha}^k dp \tag{9}$$

$$\underline{\alpha} = \sum_{k=1}^{N} \underline{\alpha}^k \tag{10}$$

where $\underline{\alpha}^k$ is the $k$-th back stress, $C_k$ and $\gamma_k$ are the model's constants to be fitted for each back stress, $d\underline{\varepsilon}^p$ is the incremental plastic strain tensor and $dp$ is the equivalent plastic strain increment.

A total of $N = 3$ back stresses were thus found to correctly fit the cyclic behaviour of the considered AlSi10Mg material, which result in a $N \cdot (C_k, \gamma_k)$ material constants. The fitted results are reported in Table 5.

**Table 5.** Fitted constants of the Chaboche model for AlSi10Mg material.

| $\sigma\|_0$ [MPa] | $C_1$ | $\gamma_1$ | $C_2$ | $\gamma_2$ | $C_3$ | $\gamma_3$ |
|---|---|---|---|---|---|---|
| 125.358 | 34,106.6 | 277.977 | 14,209.5 | 3151.75 | 7208.72 | 0.07791 |

To check the consistency of the found parameters against the experimental results, a finite element (FE) numerical model was employed. To this aim, Abaqus CAE/2018 (Abaqus 2018, Silicon Valley, CA, USA) software was employed for the numerical simulation. This consisted in a simple cube with dimensions 1 mm × 1 mm × 1 mm, which was subjected to the same strain amplitudes imposed in the experiments. The unitary cube was meshed with 20-nodes quadratic brick FE elements with reduced integration (C3D20R), with a mean size of 0.1 mm for a total of 4961 nodes and 1000 elements. The obtained numerical results are compared with those experimental in Figure 6 for each strain amplitude, in which the solid lines represent the numerical results and the points the experimental ones. The numerical elasto-plastic model was hence found to fit reasonably well with the experimental results.

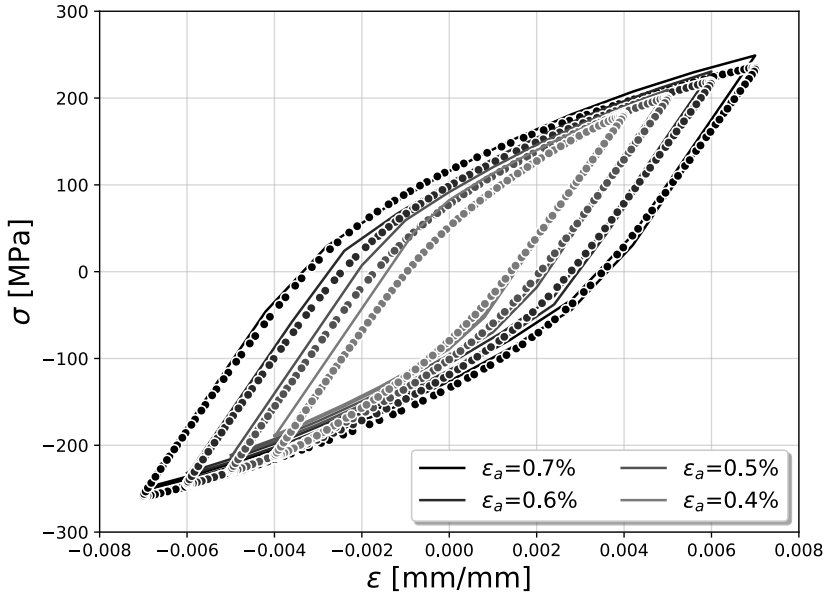


**Figure 6.** Comparison between the experimental and the numerical hysteresis cycles obtained from a FE analysis.

## 4. Stability of the Residual Stress Profile under Fatigue Loads

In previous sections it was shown that the fatigue performances of machined and sandblasted specimens were mutually comparable, while net-shape specimens showed a strong reduction for both the fatigue limit and finite life regime. It has been widely demonstrated in technical literature that the fatigue strength of AMed parts and components is mainly governed by the presence of manufacturing defects [4,53]. One can hence ascribe the different fatigue performances of the three series to different families of defects, with the net-shape showing on average the bigger defects' size.

In Section 3.4, particularly in Table 3, it was shown that all the defects found in the three series are comparable to each other. Considering the cited evidences, it is clear how an analysis merely based on the size of defects found at fracture origin is not able to justify differences in terms of fatigue behaviour observed among the three series. This section aims to introduce the presence of residual stresses in the analysis of fatigue life, focusing in particular on their evolution during a cyclic loading. This analysis was performed by means of an elasto-plastic FE model, considering the cyclic parameters found in Section 3.5.

### *4.1. Residual Stresses Approximation*

The first ingredient needed for the numerical simulation of the residual stresses relaxation is a complete stress profile along the specimen's radius. It is not practically possible to obtain a residual stress profile from the external surface to the specimen's mid-section; furthermore, from the fatigue analysis point of view, only the first material layers are particularly relevant. Due to this, the residual stresses were measured until a maximum depth of about 500 µm for the tested specimens. The residual stresses have to be self-equilibrated inside the part considered, hence a suitable model describing the complete stress profile of the material is required for the numerical simulations.

Smith et al. [46] pointed out that the residual stress field inside a cylindrical body has to guarantee the equilibrium relationships reported in Equation (11):

$$\begin{aligned} \int_0^R \sigma_{xx}^{RS}(r)dr &= 0 \\ \int_0^R r \cdot \sigma_{zz}^{RS}(r)dr &= 0 \end{aligned} \tag{11}$$

where $\sigma_{xx}^{RS}$ and $\sigma_{zz}^{RS}$ are respectively the axial and tangential residual stresses functions along the radius $r$; $R$ is the maximum radius of the considered cylinder. The expressions proposed by Smith et al. [46] were adopted for describing the residual stress field of the cylindrical specimens subjected to a mechanical material removal process, by using the value experimentally found on the external surface; the values of the residual stress in the material depth were instead computed for guaranteeing the material equilibrium. This model was here adopted to approximate the residual stress field of machined specimens, which is shown against the experimental data points in Figure 7a.

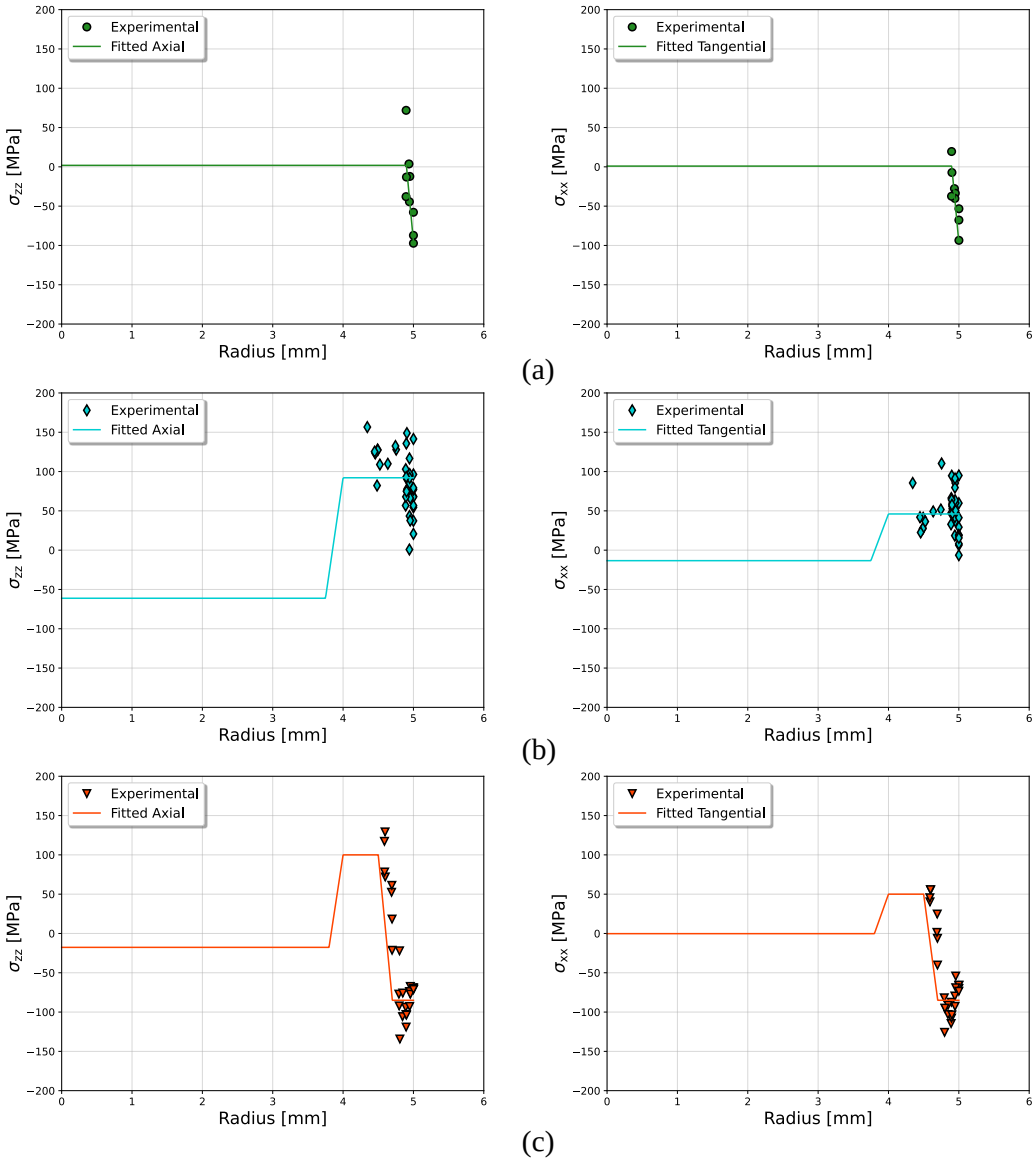


**Figure 7.** Approximation of residual stresses profile for numerical simulations against the measured data-points: (**a**) residual stress profile for machined specimens; (**b**) residual stress profile for net-shape specimens and (**c**) residual stress profile for sandblasted specimens.

Net-shape specimens showed a plateau of the residual stress behaviour from the external surface to the maximum measured depth of about 600 µm, with all of the measured values in tension. Considering this observation, the approximated function for describing the residual stress field proposed in [46], was modified to allow the definition of an initial stable behaviour of the residual stresses. The initial tensile value was supposed constant until 1 mm depth, followed by a linear decrease up to a point that guarantees the static

equilibrium of the material. The obtained approximation against the measured data point is shown in Figure 7b.

The trend of the residual stresses of the sandblasted specimens was found to be in middle between that found in machined and net-shape specimens. Furthermore, the experimental trend for these specimens was found to be in compression on the surface, followed by a slight decrease and a pseudo-linear increase in tension at the highest measured depth. This trend was hence approximated with an initial tensile stable behaviour in compression, followed by a linear increase in tension until 1 mm depth and a final linear decrease to a stress value that satisfies the relations in Equation (11). The found approximated function is showed against the experimental data points in Figure 7c. All the approximated residual stresses profiles for the three specimens' families in Figure 7 were found to fit reasonably well the experimental results, considering their typically high scatter. All the obtained profiles are self-equilibrated, resulting to be a suitable approximation, to be updated in the numerical simulations to study the residual stresses evolution during a cyclic loading.

### *4.2. Numerical Analyses*

To reduce the computational time of the cyclic elasto-plastic FE simulations, an axisymmetric model was adopted to investigate the evolution of residual stresses inside the specimens' gauge section. Only one half of the specimen was considered, a schematic of the model respect to the whole specimen's geometry is shown in Figure 8a, while its main dimension and the partitions adopted are reported in Figure 8b. The specimens' gauge section was simulated in Abaqus CAE/2018, the force and boundary conditions adopted in the model are reported in Figure 8c, and in addition to that:

- all the lower nodes lying on the x-axis were imposed to have a null displacement along the y direction, in order to be compliant with the specimen's symmetry;
- a concentrated force was applied on a reference point which is kinematically coupled to the top nodes of the model;
- all the rotations and the displacement along the x direction of the reference point were imposed to be zero.

Linear thetrahedric elements (CAX3) were adopted to mesh the model with a mean global element's size of 0.05 mm, for a total of 75,568 nodes and 149,725 elements. A detail of the FE mesh adopted in the numerical models is reported in Figure 8c. This very high mesh refinement is needed to get the numerical convergence due to the very steep variation of the residual stresses along the specimen's radius. The approximated residual stress profiles, showed in Figure 7, were updated in the FE model input file through a Python code which creates different stress fields, each associated with the corresponding node set and the value of residual stress. The updated residual stress profiles, for the different specimen's superficial states considered, at the beginning of the FE simulations are reported in Figure 9 on the left column. A total of 33 simulations were performed, 11 for each specimen's type. In each simulation the maximum alternate force was varied in order to cover the main part of the stress ranges imposed in the experimental tests, the whole set of stress ranges considered is summarised in Table 6.

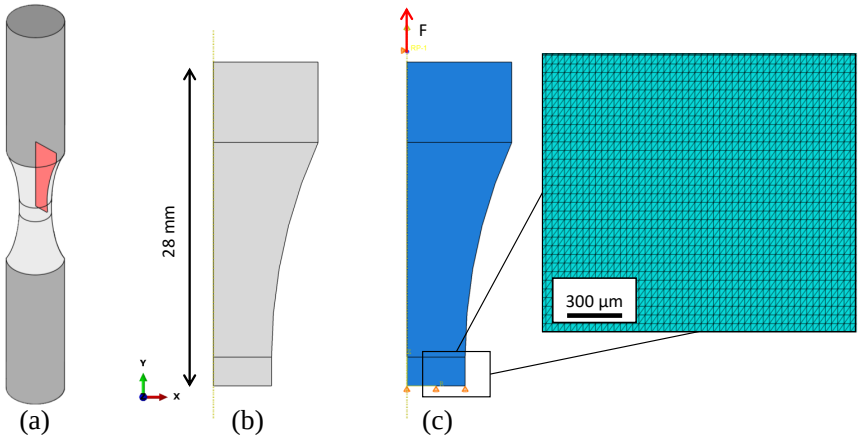


**Figure 8.** Scheme of the FE model adopted for the simulation of residual stress cyclic relaxation: (**a**) axial-symmetric model highlighted in red respect to the whole specimen; (**b**) main dimension of the part adopted in the simulation and (**c**) load, constraints and mean mesh size adopted.

Ten complete fatigue cycles were considered for each simulation at the stress levels reported in Table 6 that were found to be enough to reach the material cyclic stability. The resulting residual stress profiles at the end of the 10-th cycle are reported in Figure 9 against the nominal one for machined, net-shape and sandblasted specimens, Figure 9a, Figure 9b and Figure 9c respectively. For the sake of consistency among the residual stress profiles considered, the stress range corresponding to each curve in Figure 9 was normalized by the fatigue strength of the corresponding specimen's series (see Table 2).

**Table 6.** Summary of the stress ranges adopted for the FE simulations.

| Level | $\Delta\sigma^{\text{machined}}$ [MPa] | $\Delta\sigma^{\text{net-shape}}$ [MPa] | $\Delta\sigma^{\text{sandblasted}}$ [MPa] |
|---|---|---|---|
| 1 | 150 | 80 | 150 |
| 2 | 170 | 105 | 170 |
| 3 | 190 | 130 | 190 |
| 4 | 210 | 155 | 210 |
| 5 | 230 | 180 | 230 |
| 6 | 250 | 205 | 250 |
| 7 | 270 | 230 | 270 |
| 8 | 290 | 255 | 290 |
| 9 | 310 | 280 | 310 |
| 10 | 330 | 305 | 330 |
| 11 | 350 | 330 | 350 |

The compressive initial part of the machined specimens' residual stress profile was found to slightly relax respect to the nominal values at the fatigue limit ($\Delta\sigma/\Delta S_{\text{lim}} \sim 1$), while a strong relaxation resulted for high stress ranges, Figure 9a.

For the net-shape specimens, the residual stress profile at the end of the numerical simulation, Figure 9b, at the fatigue limit was found to mainly overlap with the nominal one, and hence, without any particular relaxation. Residual stress measurements onto a net-shape specimen tests at $\Delta\sigma = 130$ MPa for 200,000 cycles (i.e., approximately the fatigue mid-life) have confirmed this numerical prediction. On the other hand, for higher stress ranges simulations predict that the residual stress profile should relax due to because local stresses exceed the material's yield strength as highlighted in [18].

A slight relaxation, with respect to the nominal residual stress profile, happened in sandblasted specimens even near the fatigue limit (Figure 9c), with a redistribution of both the tensile and compressive parts along the specimen's radius. By applying a higher stress range, the residual stress profile resulted to be almost completely relaxed, as in the case of net-shape specimens.

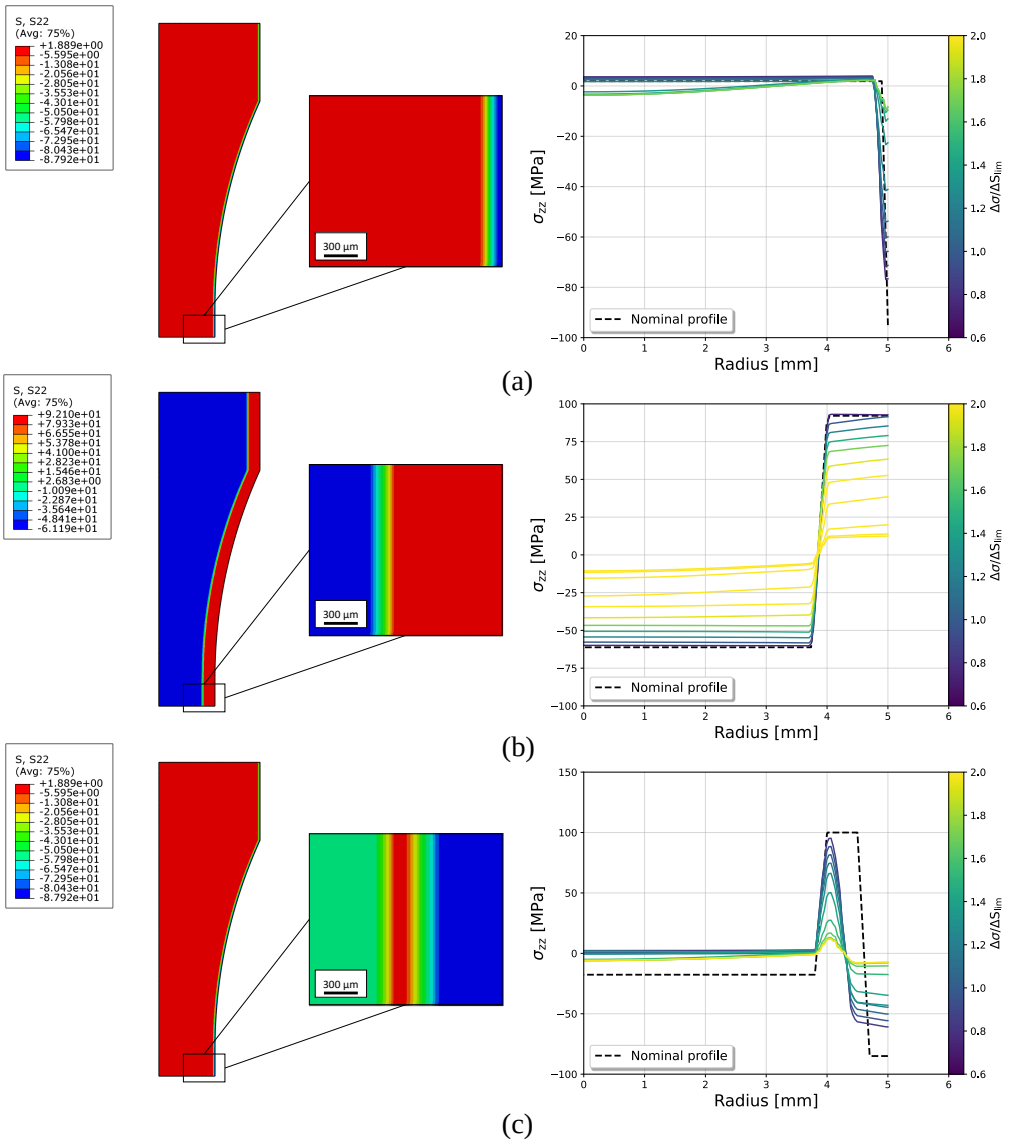


**Figure 9.** Numerical results of the simulated residual stresses relaxation for the three considered superficial states: (**a**) results of the machined specimens; (**b**) results of the net-shape specimens and (**c**) results of the sandblasted specimens. On the right the residual stresses contours at the beginning of the simulations are reported, on the left their evolution at different stress ranges.

## 5. Fatigue Model

In the previous sections it was highlighted that the fatigue performances of the AlSi10Mg are mainly governed by two factors, that are both strongly related with the superficial state considered:

1. the manufacturing defects, namely internal or superficial;
2. the presence of residual stresses, mainly compressive and tensile for machined and net-shape specimens respectively, and a mix of compressive and tensile for the sandblasted ones.

In recent published works [9,13,18], it was shown how to take into account the presence of both residual stresses and manufacturing defects in the fatigue assessment of AMed parts. A similar approach was considered here to estimate the fatigue performance in both limit and finite life regimes of the tested specimens. In addition, the effect of the residual stress relaxation due to the applied fatigue cycle, which was numerically assessed in Section 4.2, was incorporated in state-of-the-art defect-tolerant fatigue models.

### *5.1. Fatigue Strength*

One of the most used fatigue strength model able to take into account the presence of manufacturing defects is the Kitagawa-Takahashi diagram. This diagram, built with the model proposed by El Haddad [17] to take into account the effect of short cracks, has been extensively demonstrated to explain fairly well the fatigue results of AMed materials containing defects [7,8,19,54,55]. According to this model, the stress intensity factor (SIF) threshold for a general irregular crack can be estimated through Equation (12):

$$\Delta K_{\text{th}} = \Delta K_{\text{th,lc}} \cdot \sqrt{\frac{\sqrt{\text{area}}}{\sqrt{\text{area}_0} + \sqrt{\text{area}}}} \tag{12}$$

where $\Delta K_{\text{th,lc}}$ is the long crack fatigue threshold and $\sqrt{\text{area}_0}$ is the El-Haddad parameter. This value represents the dimension of the defect that separates the long crack regime from the short crack one and can be computed with Equation (13).

$$\sqrt{\text{area}_0} = \frac{1}{\pi} \cdot \left( \frac{\Delta K_{\text{th,lc}}}{Y \cdot \Delta \sigma_{\text{w0}}} \right)^2 \tag{13}$$

In Equation (13) $Y$ is the Murakami's boundary correction factor, that results $Y = 0.65$ for superficial defects and $Y = 0.50$ for the internal ones. $\Delta \sigma_{\text{w0}}$ is the fatigue limit for the defect-free material, that for fully reversed loading condition (stress ratio $R = -1.0$) can be estimated as the 0.05% of the plastic cyclic strain of the material [56]. Considering the cyclic parameters in Table 4, it can be computed as reported in Equation (14).

$$\Delta \sigma_{\text{w0}} = 2 \cdot K' \cdot (0.0005)^{n'} = 315.8 \text{ MPa} \tag{14}$$

The parameters required for the construction of the Kitagawa diagram are strongly dependent on the stress ratio at which the material is cycling, hence, they are influenced by the presence of residual stresses. This can be taken into account by adopting a NASGRO long crack threshold curve for the estimation of $\Delta K_{\text{th,lc}}$, and a Goodman model for the estimation of $\Delta \sigma_{\text{w0}}$. Additional details about the adopted models and the AlSi10Mg material parameters are reported elsewhere [13,18].

The experimental results are compared with the estimated Kitagawa curves in terms of SIF range in Figure 10, where the solid black lines are the Kitagawa curves computed considering the nominal load ratio $R_L = -1.0$. Two curves were computed for the sandblasted specimens, one for the superficial defects and another for internal ones (Figure 10c and Figure 10d respectively). The effective stress ratio can be computed considering the fatigue limit experimentally obtained (Table 2) and the value of residual stresses at a mean defect position in the specimen's depth, depending on the specimens' series considered. Two residual stress profile were considered: (a) the nominal one fitted with the experimental data and (b) the relaxed one coming from FE elasto-plastic cyclic simulations. The dashed curves with the 'x' marker are the Kitagawa curves considering the nominal residual stress profiles, while solid curves are computed from the relaxed profile from FE.

The differences between the effective curves obtained for machined, net-shape and sand blasted superficial defects with the nominal and the relaxed residual stress profiles are negligible. This is in line with the FE results in which a slight residual stress relaxation happened on the external surface of all the specimens tested near the fatigue limit. For the internal defects in sandblasted specimens, the two effective curves are, instead, very different. Furthermore, a strong underestimation of the crack threshold was obtained considering the nominal residual stress profile, while a satisfactory agreement with the experimental results was obtained considering the relaxed FE profile, Figure 10d. This happened because all the internal defects are located at about 577 µm depth from the surface, where the residual stresses undergo in a redistribution due to the cyclic load as

clearly shown by Figure 9c. Hence, at the end of the fatigue cycle the initial tensile part, results to be partially in compression, even near the specimen's fatigue limit.

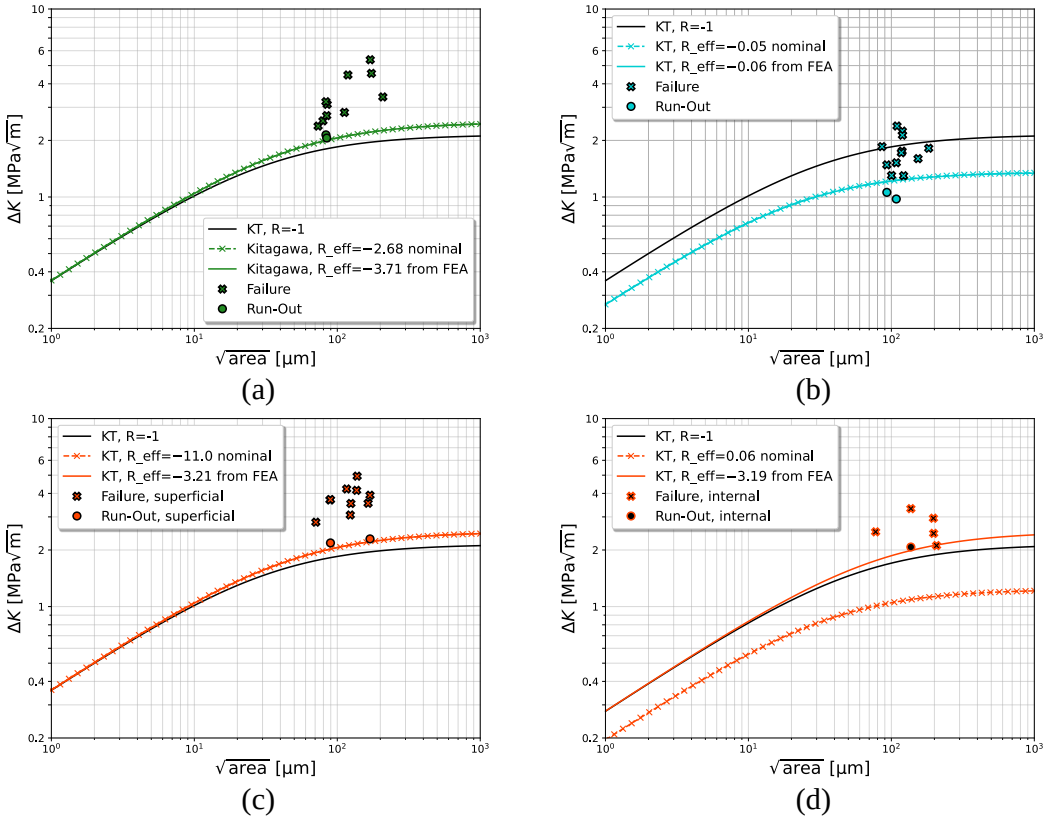


**Figure 10.** Kitagawa diagrams for the estimation of the fatigue strength against the experimental results of the three tested specimens' series: (**a**) machined specimens; (**b**) net-shape specimens; (**c**) sandblasted specimens for superficial defects and (**d**) sandblasted specimens for internal defects.

### *5.2. Finite Life Prediction*

The S-N curves were obtained numerically, by integrating the $da/dN$ NASGRO-type expression [57], Equation (15):

$$\frac{da}{dN} = C \cdot \left[ \left( \frac{1 - f_N}{1 - R_{eff}} \right) \cdot \Delta K \right]^n \cdot \left( 1 - \frac{\Delta K_{th}}{\Delta K} \right)^p$$
$$\Delta K_{th} = \Delta K_{th,lc} \cdot \sqrt{\frac{a}{a_0 + a}} \quad (15)$$

where $\Delta K$ is the SIF range, $R_{eff}$ is the effective stress ratio depending on the residual stress field and the applied load, $f_N$ is the Newman's crack opening function [58], $a$ is the crack length and $a_0$ is the El-Haddad parameter reported in Equation (13) considering the crack length instead of the square root area. $C$, $n$ and $p$ are the best fitting parameters obtained from experimental fatigue crack growth (FCG) curves, which can be found in [13].

The physical domain in which the crack propagates was approximated as a simple square with the same dimensions of the specimen's gauge section, which is a general accepted hypothesis that is also employed in commercial FCG software [59]. This hypothesis allows to calculate the SIF-range, for different applied loads and crack sizes, using the formulation proposed by Newman and Radju [60] for semi-elliptical superficial cracks propagating in finite plates. The presence of residual stresses, irrespective if they are compressive or tensile, modifies the crack opening and closure point during the propagation [61]. Furthermore, they modify the effective stress ratio during a fatigue cycle. The

effective stress ratio $R_{\text{eff}}$ changes during the crack propagation, and can be computed as reported in Equation (16):

$$R_{\text{eff}}(a,c) = \frac{K_{\min}(a,c) + K_{\text{RS}}(a,c)}{K_{\max}(a,c) + K_{\text{RS}}(a,c)} \tag{16}$$

where $K_{\min}(a,c)$ and $K_{\max}(a,c)$ are the minimum and maximum SIF reached during the fatigue loading, respectively, which were computed with the Newman-Radju model [60]; $K_{\text{RS}}(a,c)$ is the SIF due to the residual stress field in which the crack propagates. A suitable approach to compute the SIF for a crack propagating inside a general residual stress field is to use the weight function method. One of the most used weight function formulation is the one proposed by Wang and Lambert [62,63], for semi-elliptical superficial cracks propagating in a finite plate; this formulation was adopted in this work to estimate the SIF due to the residual stress field.

The initial crack sizes adopted at the beginning of the crack propagation were obtained from the defect LEVD fitted in Section 3.4, while a mean size of the crack aspect ratio $AR = a/c$ was computed from the analysis of the defects at the fracture origin of the tested specimens. Since the main part of the cracks started from the external specimen's surface, the FCG simulations were all performed under the hypothesis of superficial semi-elliptical cracks. Once fixed the crack's aspect ratio $AR$, the initial crack depth $a_{\text{i}}$ and semi-superficial initial crack length $c_{\text{i}}$ can be easily computed from the 50% percentile of the fitted LEVD, Equation (17).

$$\begin{aligned} a_{\text{i}} &= \sqrt{\frac{2 \cdot AR}{\pi}} \cdot \sqrt{\text{area}}_{50\%} \\ c_{\text{i}} &= \frac{a_{\text{i}}}{AR} \end{aligned} \tag{17}$$

The values considered for the FCG simulations for the different specimen's families are summarized in Table 7.

**Table 7.** Defect parameters adopted for the FCG simulations supposing an initial semi-elliptical crack.

| Type | $\sqrt{\text{area}}_{50\%}$ [µm] | $a/c$ | $a_{\text{i}}$ [µm] | $c_{\text{i}}$ [µm] |
|---|---|---|---|---|
| M | 114.2 | 1.000 | 91.1 | 91.1 |
| NS | 110.8 | 0.25 | 44.2 | 176.8 |
| SAB | 128.8 | 0.25 | 51.4 | 205.5 |

The failure condition that determines the end of the crack propagation was supposed to be when the crack reached a final crack depth of $a_{\text{f}} = 5.0$ mm, i.e., a half of the specimens' gauge section. Three different scenarios were considered for the FCG simulations:

- absence of residual stresses, which corresponds to the condition $R_{\text{eff}} = R_L = -1.0$;
- presence of residual stresses considering the nominal profiles fitted in Section 4.1;
- presence of residual stresses by using the values coming from the FE relaxation analyses, discussed in Section 4.2. A linear interpolation of the profiles was adopted for the values of stress range $\Delta\sigma$ outside the ones used in the FE simulations and reported in Table 6.

The obtained numerical curves are showed against the experimental results of machined, net-shape and sandblasted in Figure 11a, Figure 11b and Figure 11c respectively.

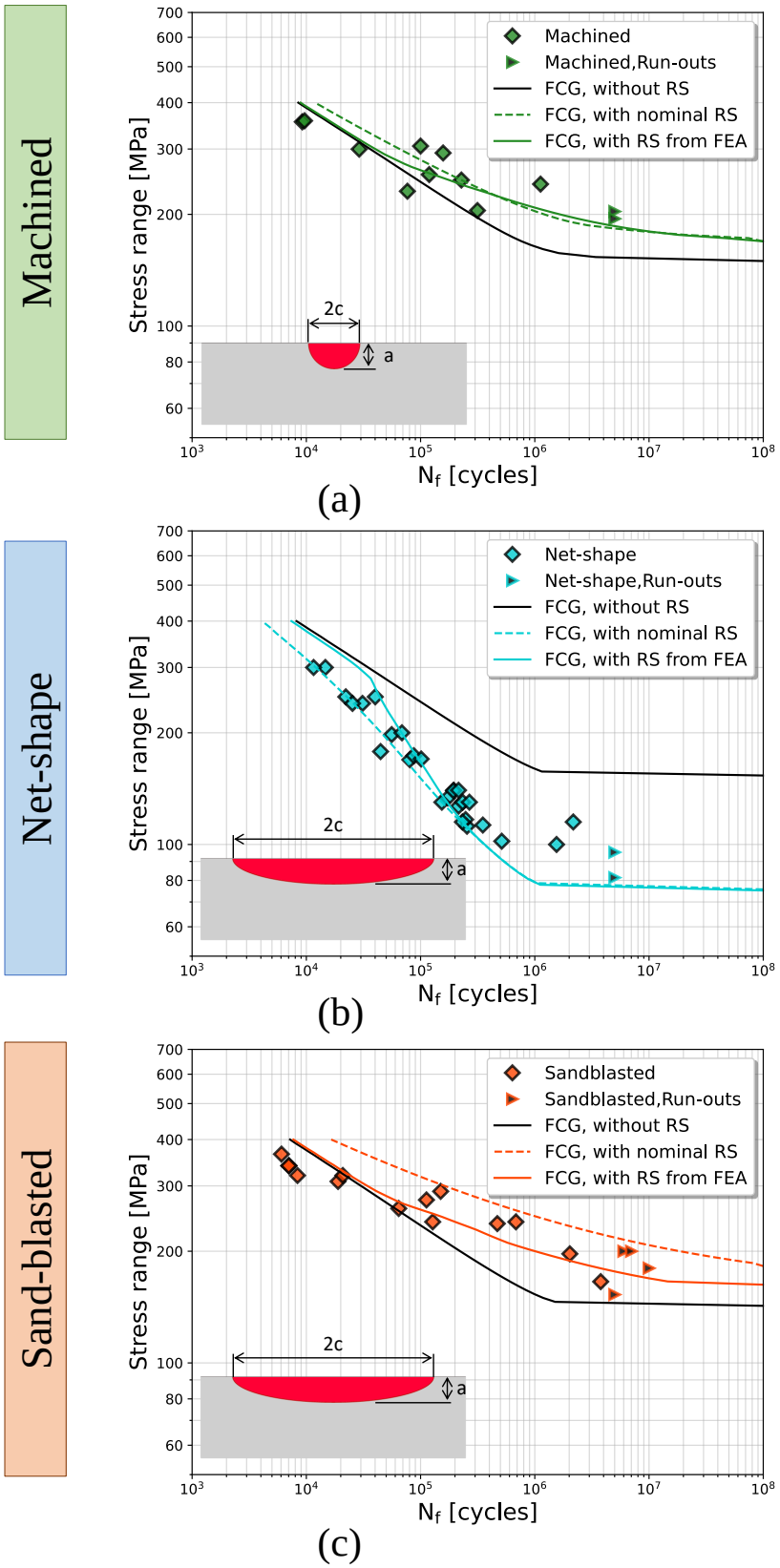


**Figure 11.** Fatigue life prediction for the different specimen's types against the experimental data-points: (**a**) S-N curves obtained for machined specimens; (**b**) S-N curves obtained for net-shape specimens and (**c**) S-N curves obtained for sandblasted specimens. For each series the 50% percentile of the defect was adopted, with a different aspect ratio $a/c$ peculiar of the surface state.

It is clear from the analysis of the results in Figure 11 that the presence of residual stresses has to be taken into account for a reliable estimation of the fatigue life. The scenario in which the residual stress field is neglected showed an underestimation (conservative) of the fatigue life respect to the experimental results for both machined and sandblasted specimens, while a strong overestimation (non conservative) resulted for the net-shape specimens. This is particularly evident in the fatigue limit regions for all the tested specimens. The scenario considering the nominal residual stress profile showed a satisfactory estimations of the fatigue life, with a loss of accuracy at the higher stress ranges. This can be ascribed to a relaxation of the residual stresses for high stress rages, as extensively discussed in Section 4.2. The best estimation of the fatigue life was, as expected, obtained considering the relaxation of the residual stresses coming from the numerical FE simulations.

## 6. Conclusions

The effect of residual stresses coming from different superficial states of the tested specimens was taken into account to evaluate the fatigue performances of AlSi10Mg alloy manufactured by L-PBF with three different surface finish conditions. A comprehensive numerical analysis, considering the elasto-plastic material behaviour, was performed to investigate the evolution of the residual stresses during a fatigue cycle and its implications in fatigue estimations. The obtained results end up to the following conclusions:

1. the different superficial states, namely machined, net-shape and sandblasted, considered in this work are characterized by significant differences in fatigue strength;
2. each specimen's series had a residual stress profile, due to manufacturing cycle, that strongly influences the fatigue behaviour;
3. a cyclic fatigue loading, even if it guarantees a global elastic behaviour of the specimens, can modify the residual stress profile. This phenomenon was investigated with a series of numerical elasto-plastic simulations;
4. accurate fatigue performances estimations were obtained by considering the real residual stresses profile from the numerical simulations of the three specimen's series and crack propagation models including short-crack and R-ratio effects;
5. the developed methodology to investigate the prospective relaxation of residual stress profiles of the fatigue specimens printed out of AlSi10Mg material seems to be promising for estimating the fatigue performances of AMed parts and components.

**Author Contributions:** (i) F.S. performed part of the fatigue tests together with the numerical analysis, he took care of the manuscript preparation; (ii) C.T. performed the residual stress measurements and part of the fatigue tests, he helped with the preparation of the original draft; (iii) S.B. directed this research activity, contributed to fatigue strength models together with preparation and revision of the manuscript. All authors have read and agreed to the published version of the manuscript.

**Funding:** Part of the tests on sand-blasted specimens were supported by Leonardo S.p.A. through research contract n. 048/21CR with the Department of Mechanical Engineering at Politecnico di Milano. Authors acknowledge support provided by MIUR Italian Ministry of Education, University and Research through the Project "Department of Excellence LIS4.0—Lightweight and Smart Structures for Industry 4.0".

**Institutional Review Board Statement:** Not applicable.

**Informed Consent Statement:** Not applicable.

**Data Availability Statement:** The data published in this paper can be requested to the corresponding author.

**Acknowledgments:** The authors acknowledge BeamIT, an Italian firm in Fornovo specialized in AM technologies and 3D printing, for supplying of the materials tested in this research activity. Authors thank Leonardo S.p.A., in the person of R. Iazurlo, for permission to publish the results of fatigue tests on sand-blasted specimens carried out within research contract n. 048/21CR.

**Conflicts of Interest:** The authors declare no conflict of interest.

## Nomenclature and Abbreviations

**Nomenclature**

| | |
|---|---|
| $a$ | Crack size |
| $A$, $B$ | Parameters of the S-N curves |
| $\alpha_k$ | $k$-th back stress of the Chaboche cyclic plasticity model |
| $c$ | Semi-superficial crack length |
| $C$, $n$, $p$ | Best fitted parameters of the NASGRO crack growth curve |
| $C_k$, $\gamma_k$ | $k$-th Chaboche cyclic plasticity model's parameter |
| $\Delta\sigma$ | Applied stress range |
| $\Delta S_{lim}$ | Fatigue stress range limit |
| $\Delta K$ | SIF range |
| $\Delta K_{th}$ | SIF range threshold |
| $E_{stab}$ | Stabilized cyclic Young's modulus |
| $\varepsilon_a$ | Alternate total strain |
| $\varepsilon_{a,el}$, $\varepsilon_{a,pl}$ | Elastic and plastic alternate strains respectively |
| $f_N$ | Newman's crack opening function |
| $K'$, $n'$ | Hardening coefficient and exponent of the Ramberg-Osgood cyclic curve |
| $K_{min}$, $K_{max}$ | Maximum and minimum SIFs respectively reached during a fatigue cycle |
| $K_{RS}$ | SIF due to the residual stress field |
| $N_f$ | Number of cycles to failure |
| $R_{eff}$ | Effective stress ratio due to the residual stress field |
| $R_\varepsilon$ | Strain ratio |
| $R_L$ | Global load ratio |
| $\sigma_a$ | Alternate stress |
| $\sigma_{xx}^{RS}$ | Tangential residual stress |
| $\sigma_{zz}^{RS}$ | Axial residual stress |
| $t$ | Depth of the superficial feature |
| $w$ | Total length of the superficial feature |
| $Y$ | Murakami's boundary correction factor |

**Abbreviations**

| | |
|---|---|
| AM | Additive manufacturing |
| AMed | Additive manufactured |
| AR | Crack aspect ratio |
| AST | American Stress Technology |
| ASTM | American Society for Testing Materials |
| FCG | Fatigue crack growth |
| FE | Finite element |
| HCF | High cycle fatigue |
| L-PBF | Laser powder bed fusion |
| LEVD | Largest extreme value distribution |
| SEM | Scanning electron microscope/microscopy |
| SIF | Stress intensity factor |
| SLM | Selective laser melting |
| S-N | Stress range over the number of cycles to failure curve |
| SPP | Spherical powder particles |
| XRD | X-ray diffraction measurements method |

## Appendix A. XRD Measurements of Residual Stresses

Hereafter are reported the residual stresses and the Full Width at Half Maximum (FWHM) with the related deviations, measured along the longitudinal ($\Theta = 0°$) and transversal ($\Theta = 90°$) directions of the sandblasted specimens. Letters A and B refer to two analysed generatrices spaced out of 180°.

**Table A1.** Measured residual stresses on sandblasted samples SAB-1 and SAB-32.

| Position | Depth [µm] | Θ = 0° Stress [MPa] | Θ = 0° Deviation [MPa] | Θ = 0° FWHM [°] | Θ = 0° Deviation [°] | Θ = 90° Stress [MPa] | Θ = 90° Deviation [MPa] | Θ = 90° FWHM [°] | Θ = 90° Deviation [°] |
|---|---|---|---|---|---|---|---|---|---|
| Specimen SAB-1 | | | | | | | | | |
| A | 0.0 | −69.0 | 4.5 | 0.74 | 0.12 | −66.4 | 4.3 | 1.68 | 0.08 |
| A | 44.3 | −67.4 | 7.2 | 1.57 | 0.08 | −54.2 | 3.2 | 1.57 | 0.10 |
| A | 105.2 | −103.1 | 15.0 | 1.50 | 0.08 | −87.5 | 12.3 | 1.47 | 0.11 |
| A | 192.9 | −134.3 | 23.6 | 1.45 | 0.08 | −95.5 | 12.3 | 1.41 | 0.09 |
| A | 303.6 | −21.4 | 8.1 | 1.42 | 0.13 | −40.2 | 11.0 | 1.40 | 0.19 |
| A | 400.6 | 71.9 | 7.9 | 1.44 | 0.11 | 55.3 | 6.8 | 1.53 | 0.23 |
| B | 0.0 | −71.3 | 4.5 | 1.74 | 0.10 | −70.0 | 4.2 | 1.69 | 0.07 |
| B | 56.0 | −73.9 | 8.6 | 1.56 | 0.08 | −79.6 | 5.9 | 1.53 | 0.08 |
| B | 109.6 | −93.9 | 15.9 | 1.50 | 0.11 | −114.6 | 9.6 | 1.41 | 0.06 |
| B | 202.6 | −92.2 | 12.1 | 1.42 | 0.12 | −125.8 | 10.2 | 1.32 | 0.08 |
| B | 304.0 | 18.3 | 13.0 | 1.44 | 0.14 | −6.2 | 10.6 | 1.40 | 0.12 |
| B | 403.2 | 129.2 | 5.2 | 1.43 | 0.11 | 55.7 | 8.7 | 1.50 | 0.17 |
| Specimen SAB-32 | | | | | | | | | |
| A | 0.0 | −70.0 | 2.4 | 1.62 | 0.10 | −65.7 | 3.9 | 1.57 | 0.08 |
| A | 44.0 | −77.3 | 13.3 | 1.41 | 0.13 | −69.1 | 4.9 | 1.49 | 0.06 |
| A | 104.0 | −119.1 | 9.5 | 1.34 | 0.14 | −107.7 | 8.8 | 1.38 | 0.08 |
| A | 155.0 | −105.8 | 17.2 | 1.35 | 0.07 | −103.1 | 8.9 | 1.31 | 0.07 |
| A | 207.0 | −77.2 | 14.9 | 1.35 | 0.10 | −81.9 | 8.7 | 1.31 | 0.06 |
| A | 311.0 | 52.4 | 7.3 | 1.35 | 0.13 | 1.4 | 9.2 | 1.35 | 0.13 |
| A | 410.0 | 78.2 | 11.8 | 1.37 | 0.13 | 40.2 | 8.8 | 1.39 | 0.18 |
| B | 0.0 | −71.2 | 2.6 | 1.65 | 0.10 | −73.5 | 3.0 | 1.60 | 0.08 |
| B | 54.0 | −92.8 | 7.3 | 1.47 | 0.06 | −92.7 | 3.1 | 1.46 | 0.06 |
| B | 99.0 | −103.8 | 14.3 | 1.44 | 0.09 | −103.6 | 6.8 | 1.38 | 0.06 |
| B | 152.0 | −75.8 | 14.8 | 1.38 | 0.11 | −91.2 | 10.1 | 1.32 | 0.08 |
| B | 198.0 | −22.1 | 10.5 | 1.36 | 0.11 | −95.0 | 11.1 | 1.31 | 0.06 |
| B | 307.0 | 61.2 | 8.9 | 1.37 | 0.12 | 24.7 | 7.0 | 1.36 | 0.12 |
| B | 412.0 | 117.2 | 5.4 | 1.39 | 0.12 | 45.4 | 8.5 | 1.43 | 0.17 |

## References


1. Gardan, J. Additive manufacturing technologies: State of the art and trends. *Int. J. Prod. Res.* **2016**, *54*, 3118–3132. [CrossRef]
2. Bandyopadhyay, A.; Bose, S. *Additive Manufacturing*; CRC Press: Boca Raton, FL, USA, 2019.
3. Tuck, C.; Hague, R.; Burns, N. Rapid manufacturing: Impact on supply chain methodologies and practice. *Int. J. Serv. Oper. Manag.* **2007**, *3*, 1–22. [CrossRef]
4. Yadollahi, A.; Shamsaei, N. Additive manufacturing of fatigue resistant materials: Challenges and opportunities. *Int. J. Fatigue* **2017**, *98*, 14–31. [CrossRef]
5. Siddique, S.; Imran, M.; Rauer, M.; Kaloudis, M.; Wycisk, E.; Emmelmann, C.; Walther, F. Computed tomography for characterization of fatigue performance of selective laser melted parts. *Mater. Des.* **2015**, *83*, 661–669. [CrossRef]
6. Siddique, S.; Awd, M.; Tenkamp, J.; Walther, F. Development of a stochastic approach for fatigue life prediction of AlSi12 alloy processed by selective laser melting. *Eng. Fail. Anal.* **2017**, *79*, 34–50. [CrossRef]
7. Romano, S.; Brückner-Foit, A.; Brandão, A.; Gumpinger, J.; Ghidini, T.; Beretta, S. Fatigue properties of AlSi10Mg obtained by additive manufacturing: Defect-based modelling and prediction of fatigue strength. *Eng. Fract. Mech.* **2018**, *187*, 165–189. [CrossRef]
8. Beretta, S.; Romano, S. A comparison of fatigue strength sensitivity to defects for materials manufactured by AM or traditional processes. *Int. J. Fatigue* **2017**, *94*, 178–191. [CrossRef]
9. Beretta, S.; Gargourimotlagh, M.; Foletti, S.; Du Plessis, A.; Riccio, M. Fatigue strength assessment of "as built" AlSi10Mg manufactured by SLM with different build orientations. *Int. J. Fatigue* **2020**, *139*, 105737. [CrossRef]
10. Du Plessis, A.; Beretta, S. Killer notches: The effect of as-built surface roughness on fatigue failure in AlSi10Mg produced by laser powder bed fusion. *Addit. Manuf.* **2020**, *35*, 101424. [CrossRef]
11. Molaei, R.; Fatemi, A.; Sanaei, N.; Pegues, J.; Shamsaei, N.; Shao, S.; Li, P.; Warner, D.; Phan, N. Fatigue of additive manufactured Ti-6Al-4V, Part II: The relationship between microstructure, material cyclic properties, and component performance. *Int. J. Fatigue* **2020**, *132*, 105363. [CrossRef]

12. Sanaei, N.; Fatemi, A. Defect-based fatigue life prediction of L-PBF additive manufactured metals. *Eng. Fract. Mech.* **2021**, *244*, 107541. [CrossRef]
13. Beretta, S.; Patriarca, L.; Gargourimotlagh, M.; Hardaker, A.; Brackett, D.; Salimian, M.; Gumpinger, J.; Ghidini, T. A benchmark activity on the fatigue life assessment of AlSi10Mg components manufactured by L-PBF. *Mater. Des.* **2021**, *218*, 110713. [CrossRef]
14. Tenkamp, J.; Koch, A.; Knorre, S.; Krupp, U.; Michels, W.; Walther, F. Defect-correlated fatigue assessment of A356-T6 aluminum cast alloy using computed tomography based Kitagawa-Takahashi diagrams. *Int. J. Fatigue* **2018**, *108*, 25–34. [CrossRef]
15. Tenkamp, J.; Awd, M.; Siddique, S.; Starke, P.; Walther, F. Fracture-mechanical assessment of the effect of defects on the fatigue lifetime and limit in cast and additively manufactured aluminum-silicon alloys from HCF to VHCF regime. *Metals* **2020**, *10*, 943. [CrossRef]
16. Murakami, Y. *Metal Fatigue: Effects of Small Defects and Nonmetallic Inclusions*; Academic Press: Cambridge, MA, USA, 2019.
17. El Haddad, M.; Topper, T.; Smith, K. Prediction of non propagating cracks. *Eng. Fract. Mech.* **1979**, *11*, 573–584. [CrossRef]
18. Sausto, F.; Carrion, P.; Shamsaei, N.; Beretta, S. Fatigue failure mechanisms for AlSi10Mg manufactured by L-PBF under axial and torsional loads: The role of defects and residual stresses. *Int. J. Fatigue* **2022**, *162*, 106903. [CrossRef]
19. Gumpinger, J.; Brandão, A.D.; Beevers, E.; Rohr, T.; Ghidini, T.; Beretta, S.; Romano, S. *Expression of Additive Manufacturing Surface Irregularities through a Flaw-Based Assessment*; ASTM International: West Conshohocken, PA, USA, 2020.
20. Edwards, P.; Ramulu, M. Fatigue performance evaluation of selective laser melted Ti–6Al–4V. *Mater. Sci. Eng. A* **2014**, *598*, 327–337. [CrossRef]
21. Leuders, S.; Thöne, M.; Riemer, A.; Niendorf, T.; Tröster, T.; Richard, H.a.; Maier, H. On the mechanical behaviour of titanium alloy TiAl6V4 manufactured by selective laser melting: Fatigue resistance and crack growth performance. *Int. J. Fatigue* **2013**, *48*, 300–307. [CrossRef]
22. Syed, A.K.; Ahmad, B.; Guo, H.; Machry, T.; Eatock, D.; Meyer, J.; Fitzpatrick, M.E.; Zhang, X. An experimental study of residual stress and direction-dependence of fatigue crack growth behaviour in as-built and stress-relieved selective-laser-melted Ti6Al4V. *Mater. Sci. Eng. A* **2019**, *755*, 246–257. [CrossRef]
23. Kruth, J.P.; Deckers, J.; Yasa, E.; Wauthlé, R. Assessing and comparing influencing factors of residual stresses in selective laser melting using a novel analysis method. *Proc. Inst. Mech. Eng. Part B J. Eng. Manuf.* **2012**, *226*, 980–991. [CrossRef]
24. Mercelis, P.; Kruth, J.P. Residual stresses in selective laser sintering and selective laser melting. *Rapid Prototyp. J.* **2006**, *12*, 254–265. [CrossRef]
25. Withers, P.J.; Bhadeshia, H. Residual stress. Part 1—Measurement techniques. *Mater. Sci. Technol.* **2001**, *17*, 355–365. [CrossRef]
26. Bartlett, J.L.; Li, X. An overview of residual stresses in metal powder bed fusion. *Addit. Manuf.* **2019**, *27*, 131–149. [CrossRef]
27. Schajer, G.S. *Practical Residual Stress Measurement Methods*; John Wiley & Sons: Hoboken, NJ, USA, 2013.
28. Shiomi, M.; Osakada, K.; Nakamura, K.; Yamashita, T.; Abe, F. Residual stress within metallic model made by selective laser melting process. *CIRP Ann.* **2004**, *53*, 195–198. [CrossRef]
29. Gouge, M.; Michaleris, P. *Thermo-Mechanical Modeling of Additive Manufacturing*; Butterworth-Heinemann: Oxford, UK, 2017.
30. Zaeh, M.F.; Branner, G. Investigations on residual stresses and deformations in selective laser melting. *Prod. Eng.* **2010**, *4*, 35–45. [CrossRef]
31. Ganeriwala, R.; Strantza, M.; King, W.; Clausen, B.; Phan, T.Q.; Levine, L.E.; Brown, D.W.; Hodge, N. Evaluation of a thermomechanical model for prediction of residual stress during laser powder bed fusion of Ti-6Al-4V. *Addit. Manuf.* **2019**, *27*, 489–502. [CrossRef]
32. Liu, Y.; Yang, Y.; Wang, D. A study on the residual stress during selective laser melting (SLM) of metallic powder. *Int. J. Adv. Manuf. Technol.* **2016**, *87*, 647–656. [CrossRef]
33. Nadammal, N.; Kromm, A.; Saliwan-Neumann, R.; Farahbod, L.; Haberland, C.; Portella, P.D. Influence of support configurations on the characteristics of selective laser-melted inconel 718. *JOM* **2018**, *70*, 343–348. [CrossRef]
34. Ali, H.; Ghadbeigi, H.; Mumtaz, K. Effect of scanning strategies on residual stress and mechanical properties of Selective Laser Melted Ti6Al4V. *Mater. Sci. Eng. A* **2018**, *712*, 175–187. [CrossRef]
35. Bagherifard, S.; Beretta, N.; Monti, S.; Riccio, M.; Bandini, M.; Guagliano, M. On the fatigue strength enhancement of additive manufactured AlSi10Mg parts by mechanical and thermal post-processing. *Mater. Des.* **2018**, *145*, 28–41. [CrossRef]
36. Ye, C.; Zhang, C.; Zhao, J.; Dong, Y. Effects of post-processing on the surface finish, porosity, residual stresses, and fatigue performance of additive manufactured metals: A review. *J. Mater. Eng. Perform.* **2021**, *30*, 6407–6425. [CrossRef] [PubMed]
37. Ngnekou, J.N.D.; Nadot, Y.; Henaff, G.; Nicolai, J.; Kan, W.H.; Cairney, J.M.; Ridosz, L. Fatigue properties of AlSi10Mg produced by additive layer manufacturing. *Int. J. Fatigue* **2019**, *119*, 160–172. [CrossRef]
38. Domfang Ngnekou, J.N.; Nadot, Y.; Henaff, G.; Nicolai, J.; Ridosz, L. Effect of As-Built and Ground Surfaces on the Fatigue Properties of AlSi10Mg Alloy Produced by Additive Manufacturing. *Metals* **2021**, *11*, 1432. [CrossRef]
39. Farajian-Sohi, M.; Nitschke-Pagel, T.; Dilger, K. Residual stress relaxation of quasi-statically and cyclically-loaded steel welds. *Weld. World* **2010**, *54*, R49–R60. [CrossRef]
40. Hensel, J.; Nitschke-Pagel, T.; Ngoula, D.T.; Beier, H.T.; Tchuindjang, D.; Zerbst, U. Welding residual stresses as needed for the prediction of fatigue crack propagation and fatigue strength. *Eng. Fract. Mech.* **2018**, *198*, 123–141. [CrossRef]
41. Lee, C.H.; Chang, K.H.; Van Do, V.N. Finite element modeling of residual stress relaxation in steel butt welds under cyclic loading. *Eng. Struct.* **2015**, *103*, 63–71. [CrossRef]

42. ASTM. *ASTM Standard E606*; Standard Test Method for Strain-Controlled Fatigue Testing. ASTM: West Conshohocken, PA, USA, 2012.
43. *ECSS-Q-ST-70-80C*; Space Product Assurance—Processing and Quality Assurance Requirements for Metallic Powder Bed Fusion Technologies for Space Applications. European Cooperation for Space Standardization: Noordwijk, The Netherlands, 2021.
44. ASTM. *ASTM E739-10*; Standard Practice for Statistical Analysis of Linear or Linearized Stress-Life (S-N) and Strain-Life (ε-N) Fatigue Data. ASTM: West Conshohocken, PA, USA, 2010.
45. Brownlee, K.; Hodges, J., Jr.; Rosenblatt, M. The up-and-down method with small samples. *J. Am. Stat. Assoc.* **1953**, *48*, 262–277. [CrossRef]
46. Smith, D.; Farrahi, G.; Zhu, W.; McMahon, C. Experimental measurement and finite element simulation of the interaction between residual stresses and mechanical loading. *Int. J. Fatigue* **2001**, *23*, 293–302. [CrossRef]
47. Schindelin, J.; Arganda-Carreras, I.; Frise, E.; Kaynig, V.; Longair, M.; Pietzsch, T.; Preibisch, S.; Rueden, C. Fiji: An open-source platform for biological-image analysis. *Nat. Methods* **2012**, *9*, 676–682. [CrossRef]
48. Murakami, Y.; Beretta, S. Small defects and inhomogeneities in fatigue strength: Experiments, models and statistical implications. *Extremes* **1999**, *2*, 123–147. [CrossRef]
49. Beretta, S.; Murakami, Y. Statistical analysis of defects for fatigue strength prediction and quality control of materials. *Fatigue Fract. Eng. Mater. Struct.* **1998**, *21*, 1049–1065. [CrossRef]
50. Beretta, S. *Affidabilità delle Costruzioni Meccaniche: Strumenti e Metodi per l'Affidabilità di un Progetto*; Springer Science & Business Media: Berlin/Heidelberg, Germany, 2010.
51. Dowling, N.E. *Mechanical Behavior of Materials: Engineering Methods for Deformation, Fracture, and Fatigue*, 4th ed.; Pearson Higher Ed.: London, UK, 2013.
52. Chaboche, J.L. Constitutive equations for cyclic plasticity and cyclic viscoplasticity. *Int. J. Plast.* **1989**, *5*, 247–302. [CrossRef]
53. Zerbst, U.; Bruno, G.; Buffiere, J.Y.; Wegener, T.; Niendorf, T.; Wu, T.; Zhang, X.; Kashaev, N.; Meneghetti, G.; Hrabe, N.; et al. Damage tolerant design of additively manufactured metallic components subjected to cyclic loading: State of the art and challenges. *Prog. Mater. Sci.* **2021**, *121*, 100786. [CrossRef] [PubMed]
54. Romano, S.; Nezhadfar, P.; Shamsaei, N.; Seifi, M.; Beretta, S. High cycle fatigue behavior and life prediction for additively manufactured 17-4 PH stainless steel: Effect of sub-surface porosity and surface roughness. *Theor. Appl. Fract. Mech.* **2020**, *106*, 102477. [CrossRef]
55. Wu, Z.; Wu, S.; Bao, J.; Qian, W.; Karabal, S.; Sun, W.; Withers, P.J. The effect of defect population on the anisotropic fatigue resistance of AlSi10Mg alloy fabricated by laser powder bed fusion. *Int. J. Fatigue* **2021**, *151*, 106317. [CrossRef]
56. Miller, K. The short crack problem. *Fatigue Fract. Eng. Mater. Struct.* **1982**, *5*, 223–232. [CrossRef]
57. SWRI. *Fatigue Crack Growth Computer Program 'NASGRO' Version 4.2*; Technical Report; Southwest Research Institute: San Antonio, TX, USA, 2004.
58. Newman, J., Jr. A crack opening stress equation for fatigue crack growth. *Int. J. Fract.* **1984**, *24*, R131–R135. [CrossRef]
59. McClung, R.C.; Enright, M.P.; Lee, Y.D.; Huyse, L.J.; Fitch, S.H. Efficient fracture design for complex turbine engine components. In *Turbo Expo: Power for Land, Sea, and Air*; ASME: New York, NY, USA, 2004; Volume 41715, pp. 291–300.
60. Newman, J., Jr.; Raju, I. An empirical stress-intensity factor equation for the surface crack. *Eng. Fract. Mech.* **1981**, *15*, 185–192. [CrossRef]
61. Beghini, M.; Bertini, L. Fatigue crack propagation through residual stress fields with closure phenomena. *Eng. Fract. Mech.* **1990**, *36*, 379–387. [CrossRef]
62. Wang, X.; Lambert, S. Stress intensity factors for low aspect ratio semi-elliptical surface cracks in finite-thickness plates subjected to nonuniform stresses. *Eng. Fract. Mech.* **1995**, *51*, 517–532. [CrossRef]
63. Wang, X.; Lambert, S. Stress intensity factors and weight functions for high aspect ratio semi-elliptical surface cracks in finite-thickness plates. *Eng. Fract. Mech.* **1997**, *57*, 13–24. [CrossRef]